The Astrophysical Journal, 574:538–553, 2002 August 1

TRIAXIAL MODELING OF HALO DENSITY PROFILES WITH HIGH-RESOLUTION *N*-BODY SIMULATIONS

Y. P. Jing
Shanghai Astronomical Observatory, Partner Group of Max-Planck-Institut für Astrophysik, Nandan Road 80, Shanghai 200030, China; ypjing@center.shao.ac.cn

and

Yasushi Suto
Department of Physics and Research Center for the Early Universe, School of Science, University of Tokyo, Tokyo 113-0033, Japan; suto@phys.s.u-tokyo.ac.jp

Received 2002 February 3; accepted 2002 April 4

ABSTRACT

We present a detailed nonspherical modeling of dark matter halos on the basis of a combined analysis of high-resolution halo simulations (12 halos with $N \sim 10^6$ particles within their virial radius) and large cosmological simulations (five realizations with $N = 512^3$ particles in a 100 h^{-1} Mpc box size). The density profiles of those simulated halos are well approximated by a sequence of the concentric triaxial distribution with their axis directions being fairly aligned. We characterize the triaxial model quantitatively by generalizing the universal density profile, that has previously been discussed only in the framework of the spherical model. We obtain a series of practically useful fitting formulae in applying the triaxial model: the mass and redshift dependence of the axis ratio, the mean of the concentration parameter, and the probability distribution functions of the axis ratio and the concentration parameter. These accurate fitting formulae form a complete description of the triaxial density profiles of halos in cold dark matter models. Our current description of the dark halos will be particularly useful in predicting a variety of nonsphericity effects, to a reasonably reliable degree, including the weak and strong lens statistics, the orbital evolution of galactic satellites and triaxiality of galactic halos, and the nonlinear clustering of dark matter. In addition, this provides a useful framework for the nonspherical modeling of the intracluster gas, which is crucial in discussing the gas and temperature profiles of X-ray clusters and the Hubble constant estimated via the Sunyaev-Zeldovich effect.

Subject headings: cosmology: theory — dark matter — galaxies: clusters: general — galaxies: halos — methods: numerical

On-line material: color figures

1. INTRODUCTION

The density profiles of dark matter halos have attracted a lot of attention recently since Navarro, Frenk, & White (1996, 1997, hereafter NFW) discovered the unexpected scaling behavior in their simulated halos. Subsequent independent higher resolution simulations (e.g., Fukushige & Makino 1997, 2001; Moore et al. 1998; Jing 2000; Jing & Suto 2000) confirmed the validity of the NFW modeling, in particular the presence of the central cusp, although the inner slope of the cusp seems somewhat steeper than they originally claimed. Those previous models, however, were based on the spherical average of the density profiles. Actually, it is also surprising that the fairly accurate scaling relation applies after the spherical average despite the fact that a departure from the spherical symmetry is quite visible in almost all simulated halos (e.g., Fig. 1 of Jing & Suto 2000).

A more realistic modeling of dark matter halos beyond the spherical approximation is important in understanding various observed properties of galaxy clusters and nonlinear clustering (especially the high-order clustering statistics) of dark matter in general. In particular, the nonsphericity of dark halos is supposed to play a central role in the X-ray morphologies of clusters (Jing et al. 1995; Buote & Xu 1997), in the cosmological parameter determination via the Sunyaev-Zeldovich effect (Birkinshaw, Hughes, & Arnaud 1991; Inagaki, Suginohara, & Suto 1995; Yoshikawa, Itoh, & Suto 1998), and in the prediction of the cluster weak lensing and the gravitational arc statistics (Bartelmann et al. 1998; Meneghetti et al. 2000, 2001; Molikawa & Hattori 2001; Oguri, Taruya, & Suto 2001; Keeton & Madau 2001). Nevertheless, useful analytical modeling of the nonsphericity is almost impossible, and numerical simulations are the only practical means of providing statistical information.

While the nonsphericity of dark matter halos is a poorly studied topic, some seminal studies do exist that attempt to detect and characterize the nonspherical signature (e.g., Barnes & Efstathiou 1987; Warren et al. 1992; Dubinski 1994; Jing et al. 1995; Thomas et al. 1998; Yoshida et al. 2000; Meneghetti et al. 2001; Bullock 2001). Nevertheless, there is no systematic and statistical study to model and characterize the density profiles of simulated halos. This is exactly what we will present in the rest of the paper. In particular, much higher mass and spatial resolutions of our current *N*-body simulations enable us to characterize the statistics of the halo nonsphericity with an unprecedented precision.

This paper is organized as follows: two different sets of *N*-body simulations that we extensively analyze here are described in § 2. In § 3, we discuss how to define the isodensity surfaces of dark matter halos from simulation data and then argue that they are well approximated by a sequence of the concentric triaxial model. Section 4 characterizes the statistical distribution of the triaxial model parameters. Finally, § 5 is devoted to summary and discussion.

2. SIMULATIONS FOR DARK MATTER HALOS

We use two different simulations for the current purpose. The first is our new set of cosmological N-body simulations with $N = 512^3$ particles in a 100 h^{-1} Mpc box, and the other is a set of high-resolution halo simulation runs. We describe the two simulations in the next subsections in order.

2.1. *Cosmological Simulations*

The first set of simulations is our new runs with $N = 512^3$ particles in a 100 h^{-1} Mpc box. These runs were carried out in 2001 with our particle-particle-particle-mesh (P^3M) code on the vector-parallel machine VPP5000 at the National Astronomical Observatory of Japan. The code adopts the standard P^3M algorithm (Hockney & Eastwood 1981; Efstathiou et al. 1985), is vectorized (Jing & Suto 1998), and has been recently parallelized. A mesh of 1200^3 grid points is used for the particle-mesh (PM) force computation with the optimized Green function (Hockney & Eastwood 1981). The short-range force is compensated for the PM force calculation at a separation less than $\epsilon = 2.7H$, where H is the mesh cell size (Efstathiou et al. 1985). The linked-list technique has been used for computing the short-range particle-particle (PP) interaction with 448^3 linked-list cells. The computer has a total of 64 processors, and we use $N_{\rm CPU} = 8$–32 processors, upon their availability, to run our code. The most important advantage of the machine for our work is that each processor has a big memory of 16 Gbyte, sufficient for storing all the information of the code. The PM computation can be easily parallelized, and it is crucial to parallelize the PP computation that dominates the CPU computation time for a strongly clustered simulation such as our present case. We sliced the simulation box in one direction (e.g., z-axis) with the thickness chosen to be the cell size of the linked-list cell. Those 448 slices in total are sorted in descending order according to the number of particles they contain. We distribute the PP force computation among the different processors in a simple way: the nth processor ($n = 1$ to $N_{\rm CPU}$) is assigned the force computation for those slices with indices of $jN_{\rm CPU} + n$, where j runs from 0 to $j_{\rm max} \equiv 448/N_{\rm CPU} - 1$. The PP interaction of the particles in the same slice and in the adjacent lower slice is considered, so the interaction for each pair of particles is computed only once. With this computation partition, we find that the load-balance problem, which becomes progressively serious for P^3M simulations in the later strongly clustered regime, can be overcome to a satisfactory degree; even at the final stage of our simulation runs, the CPU time for the PP part is nearly inversely proportional to the number of processors used. This implies that the code has achieved a good parallelization efficiency.

We consider two representative cold dark matter (CDM) models: a low-density flat cosmological model (LCDM) with $\Omega_0 = 0.3$ and $\lambda_0 = 0.7$, and the Einstein–de Sitter model with $\Omega_0 = 1$ (SCDM). The primordial density fluctuation is assumed to obey the Gaussian statistics, and the power spectrum is given by the Harrison-Zeldovich type. The linear transfer function for the dark matter power spectrum is taken from Bardeen et al. (1986). The shape and the normalization of the linear power spectrum are specified by the shape parameter, $\Gamma = \Omega_0\, h$, and σ_8, respectively, where h is the Hubble constant in 100 km s^{-1} Mpc^{-1} and σ_8 is the rms linear density fluctuation within a sphere of radius 8 h^{-1} Mpc. Table 1 summarizes the physical and simulation parameters used for these simulations. We adopted $\sigma_8 = 0.9$ for LCDM and 0.55 for SCDM, both of which are slightly smaller than those in our previous simulations (Jing & Suto 1998) but seem more consistent with recent observations (e.g., Seljak 2002; Lahav et al. 2002). With the adopted values for those physical parameters, the LCDM model satisfies almost all current observations while the SCDM model is known to have many difficulties. Therefore, we mainly analyze the LCDM model for our purpose and sometimes use the SCDM simulation just for comparison.

The box size of our cosmological simulations is 100 h^{-1} Mpc, so the particle mass is $m_p = 6.2 \times 10^8$ and 2.1×10^9 $h^{-1}\, M_\odot$, respectively, for the LCDM and SCDM simulations (Table 1). The force resolution is $\eta = 20$ h^{-1} kpc for the linear density softening form (Efstathiou et al. 1985; this roughly corresponds to $\eta/3$ for the Plummer-type softening length). The simulations are evolved by 1200 time steps from the initial redshift $z_i = 72$. Two realizations are computed for each model. One additional LCDM simulation (LCDMa) uses a smaller force softening $\eta = 10$ h^{-1} kpc and is evolved with 5000 time steps in order to check the possible effect of the force softening on the final dark matter distribution especially at small scales. As far as the shape of the virialized halos is concerned, we made sure that both simulations (LCDM and LCDMa) yield almost identical results. In what follows, therefore, we do not distinguish between LCDM and LCDMa and simply refer to them as LCDM.

2.2. *Identification of Dark Halos in the Cosmological Simulations*

The friends-of-friends (FOF) method is a widely used algorithm to identify dark matter clumps in N-body data. The mean overdensity within the clumps is approximately proportional to b^{-3}, where b is the bonding length. It has been shown that the FOF clumps with $b = 0.2\bar{d}$, where $\bar{d} \equiv L/N^{1/3}$ is the mean separation of particles, approximately correspond to the virialized dark matter halos of mean overdensity 180 (e.g., Davis et al. 1985; Lacey & Cole 1994). On the other hand, a large fraction of the FOF clumps identified with $b = 0.2\bar{d}$ are known to form a system of multiple virialized halos that are bridged via thin filaments (e.g., Suto, Cen, & Ostriker 1992; Suginohara & Suto

TABLE 1

MODEL PARAMETERS FOR COSMOLOGICAL SIMULATIONS WITH $N = 512^3$ IN A 100 h^{-1} Mpc BOX

Model	Ω_0	λ_0	σ_8	Γ	m_p ($h^{-1}\, M_\odot$)	η (h^{-1} kpc)	Time Steps	Realizations
LCDM.....	0.3	0.7	0.9	0.2	6.2×10^8	20	1200	2
SCDM.....	1.0	0.0	0.55	0.5	2.1×10^9	20	1200	2
LCDMa.....	0.3	0.7	0.9	0.2	6.2×10^8	10	5000	1

1992; Jing & Fang 1994, hereafter JF94). JF94 proposed to compute the overdensity around the local potential minima within each FOF clump to separate the virialized halos. While this can effectively achieve the goal, it is time consuming to find the local potential minima (because there may be multiple minima within a single FOF clump).

Here we propose to use an alternative method that works faster. The thin bridges connecting the halos identified with $b = 0.2\bar{d}$ can be effectively eliminated by reducing b. By trial and test, we found that the thin bridges almost disappear if we adopt $b = 0.1\bar{d}$. With this recipe, however, the resulting FOF clumps have a smaller size and a higher overdensity than those defined according to the spherical collapse model. Therefore, our scheme should be interpreted to identify first the central parts or the substructures of the entire halo. Next, for each FOF clump of $b = 0.1\bar{d}$, we compute the gravitational potential of every member particle. The position of the particle of the minimum potential is defined as the center of the hosting halo. Then the spherical overdensity is computed around the halo center with increasing the radius, and the virial radius $r_{\rm vir}$ is found when the overdensity reaches the value predicted in the spherical collapse model. Here we use the fitting formula of Bryan & Norman (1998) for the spatially flat $[\Omega(z) + \lambda(z) = 1]$ models:

$$\Delta_{\rm vir}(z) \equiv \frac{3M_{\rm vir}}{4\pi r_{\rm vir}^3 \rho_{\rm crit}} = 18\pi^2 + 82[\Omega(z) - 1] - 39[\Omega(z) - 1]^2 , \quad (1)$$

where $\rho_{\rm crit}$ is the critical density of the universe. Since our choice $b = 0.1\bar{d}$ preferentially selects smaller clumps than those predicted in the spherical model, some fraction of such clumps turn out to be substructures within the virial radius of a larger halo defined in the above equation. If the virial spheres of more than one halo overlap, we simply retain the most massive clump and throw away the others from the final halo list.

2.3. *High-Resolution Halo Simulations*

Our cosmological simulations that we described above have a sufficient spatial resolution to discuss the statistics concerning the halo shapes and the concentration of the density profile (§§ 4 and 5) as was conducted by Jing (2000) in the framework of the spherical approximation. Actually, except for the delicate problem of determining the slope of the central cusp at $r \ll 0.01 r_{\rm vir}$, a larger simulation volume is more important than higher resolution for the current purpose. Nevertheless, we also use our higher resolution halo simulations (Jing & Suto 2000; hereafter simply referred to as halo simulations) to demonstrate that our triaxial modeling indeed provides a better description for halo profiles than the conventional spherical modeling (§ 3).

These halos are simulated with about a million particles within their virial radii (see Table 1 of Jing & Suto 2000). For mass scales of clusters, groups, and galaxies, there are four halos, respectively, and thus 12 halos in total. They are simulated in the LCDM model except the fact that the fluctuation amplitude, $\sigma_8 = 1$ (Kitayama & Suto 1997), is a bit larger than our current choice $\sigma_8 = 0.9$. Another advantage of the halo simulations is that those halos are simulated with almost an equal number of particles independently of the mass of the halos, and thus the resolution relative to the virial radius and the halo mass is kept constant. This is not the case for the cosmological simulations in which massive halos would have a better resolution in terms of the number of particles involved. Thus, the possible artificial effect due to the variable resolution is suppressed in the halo simulations.

TABLE 2

PROPERTIES OF THE NEW SIMULATED HALOS IN THE LCDM MODEL WITH $\Omega_0 = 0.3$, $\lambda_0 = 0.7$, $h = 0.7$, $\sigma_8 = 1$, AND $\Gamma = 0.21$

Identification Number	M[a] ($h^{-1} M_\odot$)	N_p[b]	$r_{\rm vir}$[c] (h^{-1} Mpc)
GX 5	6.1×10^{12}	945,864	0.373
GR 5	5.5×10^{13}	644,839	0.776

[a] Mass of the halo within its virial radius.
[b] Number of particles within its virial radius.
[c] The virial radius of the halo.

After Jing & Suto (2000) was published, we completed runs of two additional halos with a galactic mass and with a group mass. Those new halos are referred to as GX 5 and GR5, respectively, according to our previous convention (see Table 2). While we add these two, we also eliminate two previous halos from the list of halos that we examine below: GR2, which shows a clear bimodal structure, and GX 1, which is seriously disrupted at $z \leq 0.5$ because of the tidal force of a nearby massive object. This is because the major purpose of analyzing the halo simulation catalogs is to check the validity of the triaxial modeling for typical halos. The fraction of those atypical halos is properly taken into account in the statistics drawn from the cosmological simulations. Thus, the above replacement does not bias our conclusion.

3. MODELING THE NONSPHERICAL DENSITY PROFILES OF DARK MATTER HALOS

In this section, we propose that a nonsphericity in the density profiles of dark halos is well described by a triaxial model on the basis of the detailed analysis of the halo simulations. In fact, we demonstrate that the triaxial modeling significantly improves the fit to the simulated profiles, at least for relatively relaxed halos, compared to the conventional spherical model. The statistical description including the probability distribution functions for axis ratios and the concentration parameters will be discussed in the next section using the cosmological simulations.

3.1. *Defining the Isodensity Surfaces inside Individual Halos*

The shapes of dark halos have been previously studied by many authors (e.g., Barnes & Efstathiou 1987; Warren et al. 1992; Jing et al. 1995; Thomas et al. 1998), and it is already well known that they exhibit a significant amount of departure from spherical distribution. Those previous studies first compute the inertial tensor for each halo and then compute the distribution of the axial ratios and the correlation of the direction of the principal axes. While this is a well-defined method of characterizing the shape of halos in principle, we do not employ it for two reasons.

First, this method assumes that we know *in advance* which particles belong to each halo. In reality, this is not the case since we usually attempt to determine the member particles of a halo and its shape simultaneously. This is serious because the inertia tensor is sensitive to the outer boundary

of the halo where the membership of particles is also difficult to define. Previous studies get around the problem by applying the procedure iteratively: first, all particles within a certain spherical radius from the center of the halo are included to compute the inertial tensor and the resulting ellipsoidal configuration. Next, those particles outside the ellipsoid are thrown away from the member particles of the halo, and the inertia tensor is recalculated. This procedure is repeated until the solution converges. While this method seems to work well in previous low-resolution N-body data, we were not able to obtain a good convergence in the case of our high-resolution halos. This is ascribed to the fact that our high-resolution halos retain a significant amount of substructures that have been artificially erased because of the *overmerging* effect in previous lower resolution simulations. The iteration procedure is not stable in the presence of significant substructures especially at the boundary region of halos, since the inertial tensor is quite sensitive to them.

Second, our main interest here is not simply to define the overall shape of halos but to characterize the density profile. Therefore, we would like to have a sequence of *isodensity* surfaces with different overdensities. The ellipsoidal surface obtained from the above procedure, even if it converges, is not related to those isodensity surfaces and thus not so useful after all for our purpose here.

With the above problems of the previous method in mind, we propose another approach to find the isodensity surfaces. This begins with the computation of a local density at each particle's position. We adopt the smoothing kernel widely employed in the smoothed particle hydrodynamics method (e.g., Hernquist & Katz 1989):

$$W(r,h_i)=\frac{1}{\pi h_i^3}\begin{cases}1-\frac{3}{2}\left(\frac{r}{h_i}\right)^2+\frac{3}{4}\left(\frac{r}{h_i}\right)^3 & (r\le h_i)\\ \frac{1}{4}\left(2-\frac{r}{h_i}\right)^3 & (h_i<r<2h_i)\\ 0 & \text{otherwise}\ ,\end{cases} \tag{2}$$

where h_i is the smoothing length for the ith particle. We use 32 nearest neighbor particles to compute the local density ρ_i, and h_i is set to be one-half the radius of the sphere that contains those 32 neighbors. Using ρ_i, we construct the isodensity surfaces corresponding to the five different thresholds:

$$\rho_s^{(n)}=A^{(n)}\rho_{\rm crit}\ , \tag{3}$$

$$A^{(n)}=100\times 5^{n-1}\quad (n=1\sim 5)\ . \tag{4}$$

In practice, we collect all particles satisfying $0.97\rho_s^{(n)}<\rho_i<1.03\rho_s^{(n)}$ to define the nth isodensity surface. The typical sizes (the mean radii) of those surfaces are 0.6, 0.4, 0.25, 0.12, and 0.06 times the virial radius of the halo, respectively. Note that $\rho_s^{(n)}$ is the *local* density, and thus the *mean* density of the halo inside the corresponding radius of $\rho_s^{(n)}$ is generally much higher.

Actually, a straightforward application of equation (3) results in many small distinct regions with the identical density threshold inside an individual halo. This is again due to the presence of the strong substructures in the halo. Since we are interested in the isodensity surfaces that represent the overall density profile of the parent halo, we have to eliminate those small regions corresponding to the substructures. For this purpose, we again use the FOF technique but with a different bonding length from that we used when identifying the virialized halos. After some trial and error, we find that an adaptive (i.e., dependent on each isodensity value) bonding length of $b_n=3(\rho_s^{(n)}/m_p)^{-1/3}$ works well (cf. Suto et al. 1992).

3.2. *Triaxial Model Fits to the Isodensity Surfaces*

Figure 1 plots typical examples of the projected particle distributions within the isodensity surfaces for four different halos (CL3, GR1, GR5, and GX 3) after particles in strong substructures are eliminated as described above. Those plots clearly suggest that the isodensity surfaces are typically approximated as triaxial ellipsoids. Thus, we performed the following triaxial fit to the isodensity surfaces with five different thresholds separately:

$$R^2(\rho_s)=\frac{X^2}{a^2(\rho_s)}+\frac{Y^2}{b^2(\rho_s)}+\frac{Z^2}{c^2(\rho_s)}\ . \tag{5}$$

The origin of the coordinates is always set at the center of mass of each surface, and the principal vectors $\boldsymbol{a}$, $\boldsymbol{b}$, and $\boldsymbol{c}$ ($a\le b\le c$) are computed by diagonalizing the inertial tensor of particles in the surface (Fig. 2). The projected views of the corresponding fitted ellipsoids are shown in the bottom panels of Figure 1, which imply that the ellipsoid fitting is a good approximation (at least visually).

Figure 3 plots the dependence of the axis ratios, a/c and b/c, on the isodensity threshold ρ_s. Naturally, each halo exhibits different behavior that may reflect the different merging history and/or tidal force field. Nevertheless, several systematic dependences are quite visible. The halos of cluster mass generally have smaller axial ratios than those of galactic mass, implying that the halos of the galactic mass are rounder on average than those of cluster mass. This mass dependence will be quantified with a large sample of halos from the cosmological simulations in § 4.

On the other hand, we also note that the axial ratios decrease with increasing density; the isodensity surfaces become more elongated in the central region than in the outer region. The mean (with the error bar of the mean) of the axial ratios computed from the 12 halos are plotted in the right panels of Figure 3 (*symbols*). The solid lines show the single power-law fit for the mean axis ratios:

$$\frac{a}{c}=0.56\left(\frac{\rho_s/\rho_{\rm crit}}{2500}\right)^{-0.052} \tag{6}$$

$$\frac{b}{c}=0.71\left(\frac{\rho_s/\rho_{\rm crit}}{2500}\right)^{-0.040}\ . \tag{7}$$

Figure 4 shows the degree of alignment of the axis directions among isodensity surfaces at different densities (radii). We define θ_{11} as the angle between the major axis of the isodensity surfaces and that of the $A^{(3)}=2500$ isodensity surface as shown in Figure 2. Similarly, θ_{22} is defined with respect to their middle axes. According to our definition, $\cos\theta_{11}=\cos\theta_{22}=1$ at $\rho_s/\rho_{\rm crit}=A^{(3)}=2500$.

We find that the major axes align pretty well within a halo; for about 70% of the halos $\cos\theta_{11}$ at different radii is larger than 0.7. For about one-half of the sample, $\cos\theta_{11}$ is larger than 0.9. In a few cases (three of 12 halos), however, the alignment of the major axes is poor. When we check

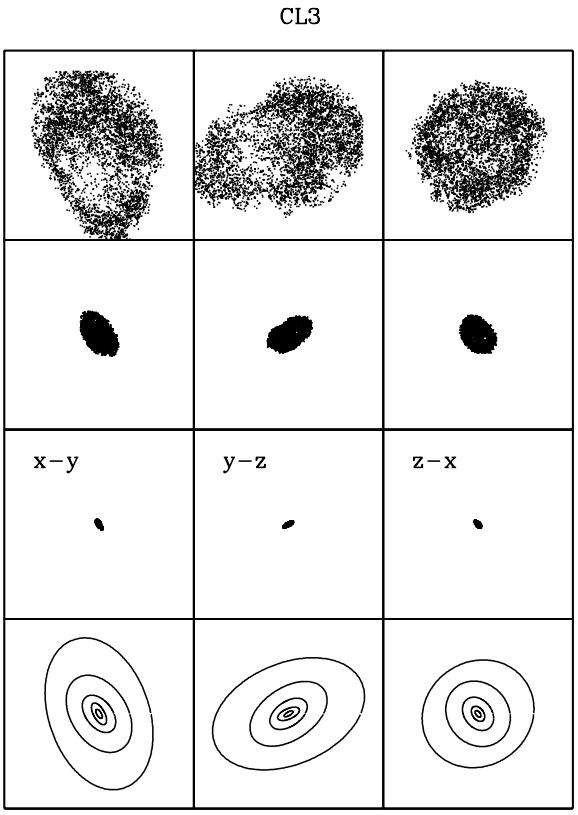

FIG. 1*a*

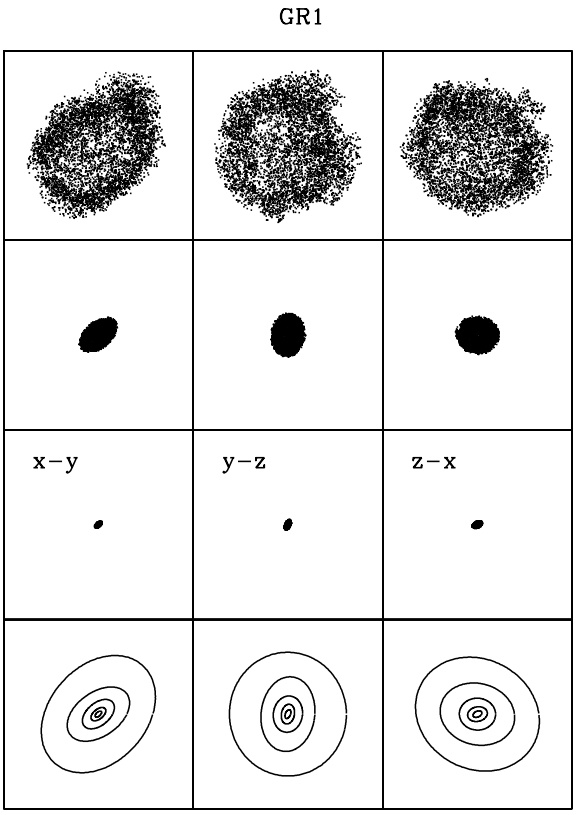

FIG. 1*b*

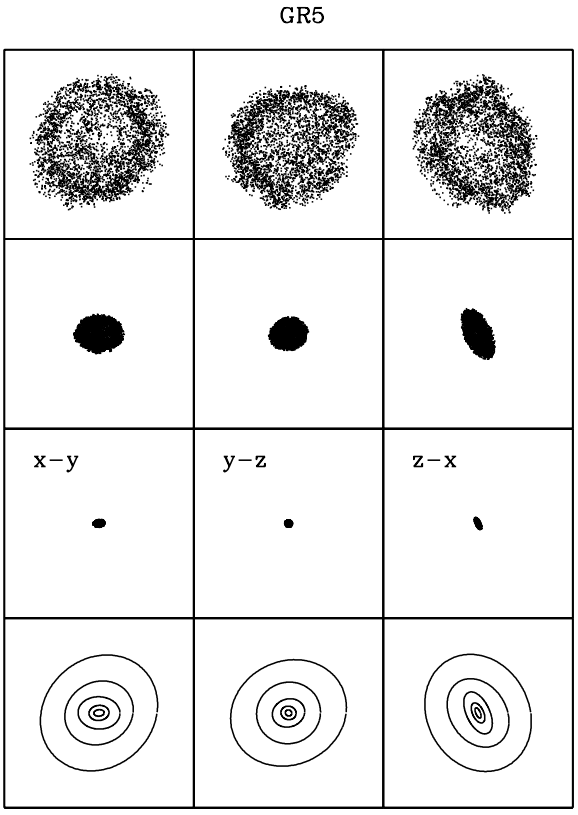

FIG. 1*c*

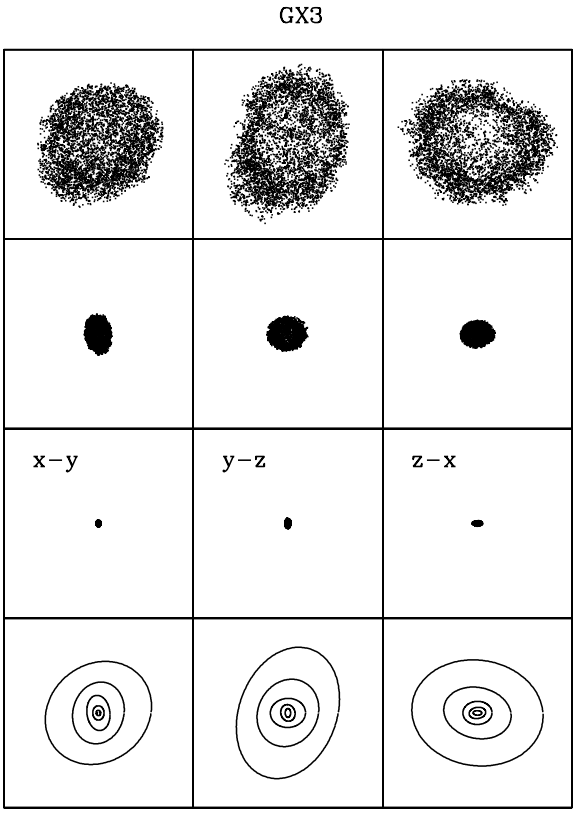

FIG. 1*d*

FIG. 1.—Examples of projected particle distribution in four halos: (*a*) CL3, (*b*) GR1, (*c*) GR5, and (*d*) GX 3. The size of each box is $2r_{\rm vir}$ of each halo. For each halo, particles in the isodensity shells with $A \equiv \rho_s/\rho_{\rm crit} = 100$, 2500, and 6.25×10^4 are plotted on the (x, y)-, (y, z)-, and (z, x)-planes (*from left to right*). The bottom panels show the triaxial fits to five isodensity surfaces projected on those planes.

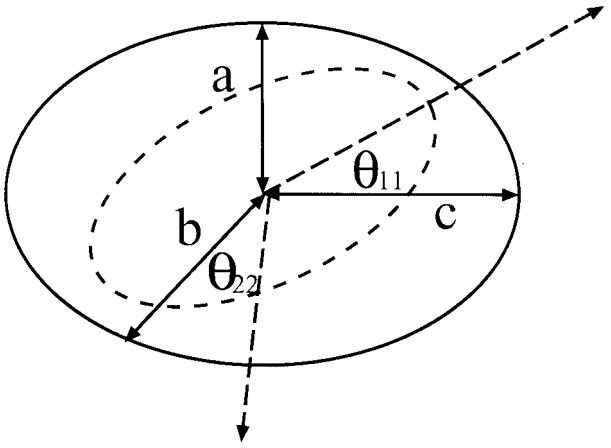

FIG. 2.—Schematic illustration of the triaxial model for the isodensity surface of dark matter halos. The axis lengths are defined to be $a \leq b \leq c$, and θ_{11} (θ_{22}) measures the angle between the longest (middle) axis of the isodensity surface with that of $A^{(3)} = 2500$ (eq. [4]).

these halos individually (e.g., GR1), it turns out that b/c for the two halos is quite close to unity, indicating that they are oblate halos with $b \approx c$ and thus the direction of the major axis is difficult to measure (if $b = c$, the direction of the major axis is arbitrary within a plane). Thus, the apparent misalignment of their major axes is not meaningful. Only for the one remaining halo (GX 3; Fig. 1), the major axes of the outer and the innermost isodensity surfaces are indeed perpendicular to that at the middle. This is the real case where the major axes are significantly misaligned.

The alignments of the middle axes show similar behavior: for most of the halos the degree of alignment is satisfactory. For those that show significant misalignment of the middle axes, their a/b or b/c ratio is usually quite close to unity and the direction of the middle axes (and the minor or major axes) can be poorly determined at best. It is only in a case like GX 3 that no simple ellipsoid description can be found,

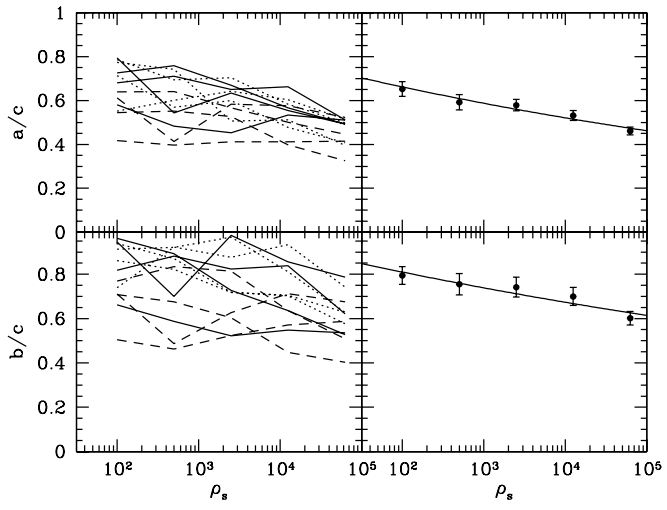

FIG. 3.—Axis ratios for the triaxial model fits to 12 halos. *Left:* Results for individual halos. The dashed lines are for cluster halos, the dotted lines for group halos, and the solid lines for galactic halos. *Right:* Symbols indicate the mean and its 1 σ error from the halo simulations, while the solid lines show the single power-law fit (eq. [6]). The upper and lower panels show a/c and b/c, respectively. [*See the electronic edition of the Journal for a color version of this figure.*]

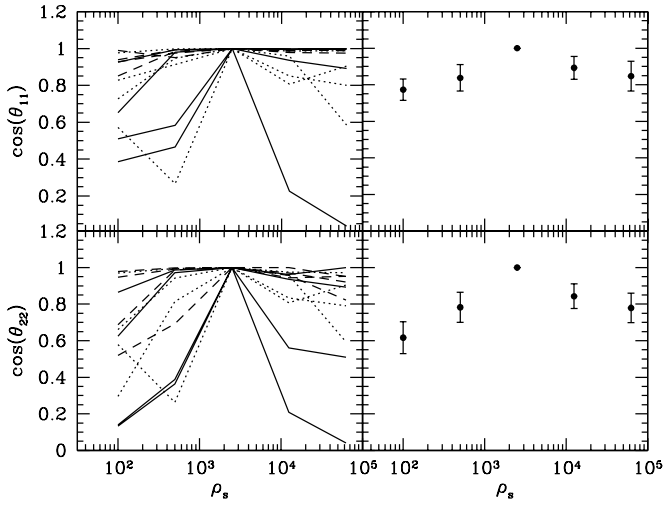

FIG. 4.—Degree of alignment of the directions of the ellipsoid axes. *Left:* Results for individual halos. The dashed lines are for cluster halos, the dotted lines for group halos, and the solid lines for galactic halos. *Right:* Symbols indicate the mean and its 1 σ error from the halo simulations. The upper and lower panels show for the major and middle axes, respectively. [*See the electronic edition of the Journal for a color version of this figure.*]

but this is fairly exceptional. The alignment seems slightly better for cluster-sized halos, but this would be simply because galactic halos are more spherical and thus the direction of the major axis is less accurate than that for cluster-sized halos.

3.3. *Triaxial versus Spherical Modeling of Dark Halos*

In the last subsection, we have seen that the isodensity ellipsoids at different radii are approximately aligned and the axial ratios of the ellipsoids are nearly constant. These facts suggest the possibility that the internal density distribution within a halo can be approximated by a sequence of concentric ellipsoids of constant axis ratio. To show this to be an improved description over the conventional spherical description, we compute the quadrupole of the particle distribution within a spherical shell (Q_s) or an ellipsoid shell (Q_e). For a spherical shell, the positions of particles inside the shell can be described by

$$\begin{cases} x = r \sin\theta \cos\phi \\ y = r \sin\theta \sin\phi \\ z = r \cos\theta \end{cases}, \tag{8}$$

with r being the (conventional) spherical radius. Similarly, the positions of the particles in an ellipsoidal shell can be described by

$$\begin{cases} X = R\left(\dfrac{a}{c}\right) \sin\Theta \cos\Phi \\ Y = R\left(\dfrac{b}{c}\right) \sin\Theta \sin\Phi \\ Z = R \cos\Theta \end{cases}, \tag{9}$$

where X-, Y-, and Z-axes are the principal vectors of the ellipsoidal shell and a/c and b/c are the axis ratios. In the rest of the paper, we preferentially use the capital R to refer to the length of the major axis defined in the triaxial model.

Then the quadrupole moments of the isodensity surfaces in the spherical and triaxial models, Q_s and Q_e, are com-

puted as

$$Q_s \equiv \frac{1}{5N_p}\sum_{m=-2}^{+2}\left|\sum_j Y_{2m}(\theta_j,\phi_j)\right|^2 - 1 \ , \qquad (10)$$

$$Q_e \equiv \frac{1}{5N_p}\sum_{m=-2}^{+2}\left|\sum_j Y_{2m}(\Theta_j,\Phi_j)\right|^2 - 1 \ , \qquad (11)$$

where the summation over j runs for all particles (N_p) in the isodensity surface and Y_{lm} is the spherical harmonics. If the spherical (triaxial) model is exact, Q_s (Q_e) vanishes. Using these measures, we will show the extent to which the triaxial model indeed provides a significantly improved description for the simulated halos.

In practice, we compute $Q_s(r)$ and $Q_e(R)$ for five shells of each halo at $r = R = 0.65r_{\rm vir}$, $0.35r_{\rm vir}$, $0.2r_{\rm vir}$, $0.12r_{\rm vir}$, and $0.065r_{\rm vir}$ with the shell thickness $\Delta r/r = \Delta R/R = \ln 10 \times 0.1 = 0.23$. Those shells are centered at the potential minimum of the halo. In the triaxial model, we assume that *the shells have the same axis ratios and the same principal axis directions as measured from the isodensity surface at* $A^{(3)} = 2500$. Thus, those shells do not necessarily correspond to the isodensity surfaces that we have discussed. Actually, this treatment is important because otherwise the triaxial model (with more degrees of freedom) should always provide a better fit. In addition, this approximation is most likely what one would like to apply statistically to halos of visible objects, which would yield a practical and fair comparison between the spherical and triaxial models.

In the top and middle panels of Figure 5, we present the quadrupole moments Q_s and Q_e for the 12 halos. The quadrupole Q_s for the spherical modeling increases nearly monotonically with the radius. The Q_e for our ellipsoidal modeling (in its simplified version as described above) stays flat at $R < 0.3r_{\rm vir}$ but increases with the radius at the larger radius. The ratio of the two quadrupoles is shown in the bottom panel of Figure 5, which indicates that our triaxial model, even simplified, fits the simulated halo profiles much better than the spherical model. For 10 of 12 halos, the ratio, $Q_e(R)/Q_s(r)$, is much smaller than 1 at all scales ($r = R$). Even for the remaining two halos (GX 3 and GR5), the ratio exceeds unity a bit only at the largest radius, and the triaxial description shows a significant improvement over the spherical model. The ratio $Q_e(R)/Q_s(r)$ seems to approach unity as r becomes closer to $r_{\rm vir}$. The reason might be that the subclustering is more prominent in the outskirt region than in the central region, since the subhalos are tidally stripped when they fall into the central region (see Fig. 1 of Jing & Suto 2000). The strong subclustering makes it difficult for both the spherical model and the ellipsoidal model to accurately describe the complicated density distribution at $r_{\rm vir}$. However, the figure also clearly shows that our triaxial model works significantly better than the spherical model for $r < 0.7r_{\rm vir} \approx r_{200}$, i.e., almost the entire halo (the definition for r_{200} will be given shortly).

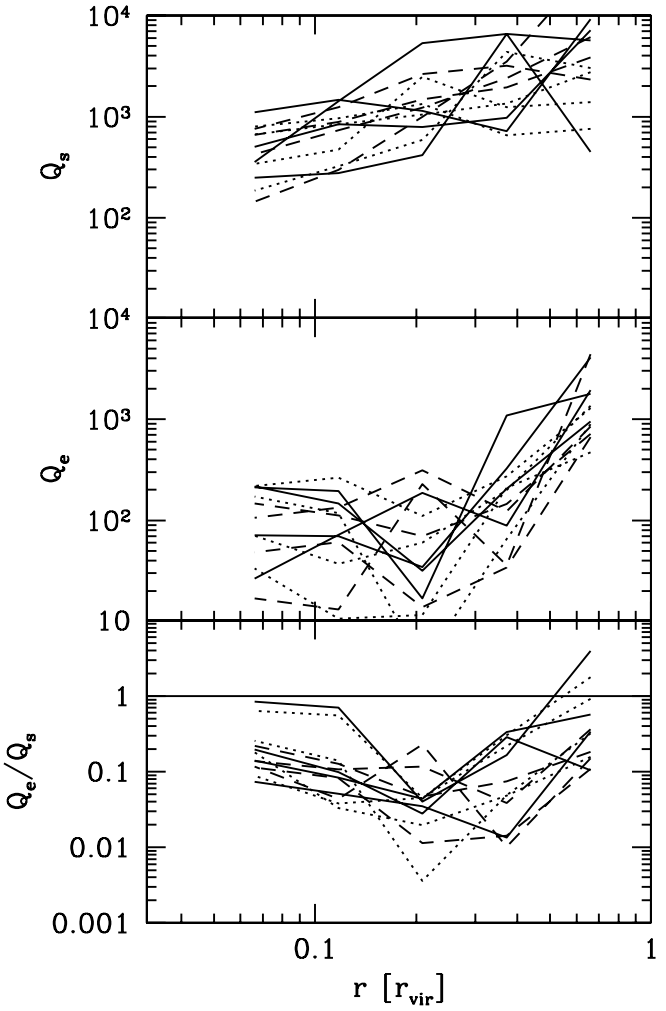

FIG. 5.—Quadrupole moments defined in the triaxial model (Q_e) and in the spherical model (Q_s) for five shells at radii from $0.05r_{\rm vir}$ to $0.65r_{\rm vir}$. They are presented in the top two panels, and their ratio Q_e/Q_s is in the bottom panel. The dashed lines are for cluster halos, the dotted lines for group halos, and the solid lines for galactic halos. [*See the electronic edition of the Journal for a color version of this figure.*]

3.4. *Density Profiles in the Triaxial Model*

The next important task is to describe the density profiles in the triaxial model generalizing the previous results in the spherical approximation (NFW; Moore et al. 1998; Jing & Suto 2000; Klypin et al. 2001). In the same spirit as the previous subsection, we do not perform the fit to the isodensity surfaces that we identified but rather compute the mean density $\rho(R)$ at the simplified triaxial shells (i.e., the same axis ratios and axis directions for the entire halo as those measured from its isodensity surface at $A^{(3)} = 2500$) within a thickness of $\Delta R/R = 0.12$.

Figure 6 plots the density profiles measured in this way for individual halos as a function of R. As in the spherical case, we adopt the following form:

$$\frac{\rho(R)}{\rho_{\rm crit}} = \frac{\delta_c}{(R/R_0)^{\alpha}(1+R/R_0)^{3-\alpha}} \ , \qquad (12)$$

where R_0 is a scale radius and δ_c is a characteristic density. Again following the definition of r_{200} in the spherical model (within which the mean matter density is $200\rho_{\rm crit}$), we define a radius R_e so that the mean matter density within the ellipsoid of the major axis radius R_e is $\Delta_e\rho_{\rm crit}$ with

$$\Delta_e = 5\Delta_{\rm vir}\left(\frac{c^2}{ab}\right)^{0.75} \ . \qquad (13)$$

The nontrivial dependence of Δ_e on the axis ratios in the above equation is chosen so that R_e becomes a fixed fraction of the virial radius $r_{\rm vir}$ (see Fig. 7 below).

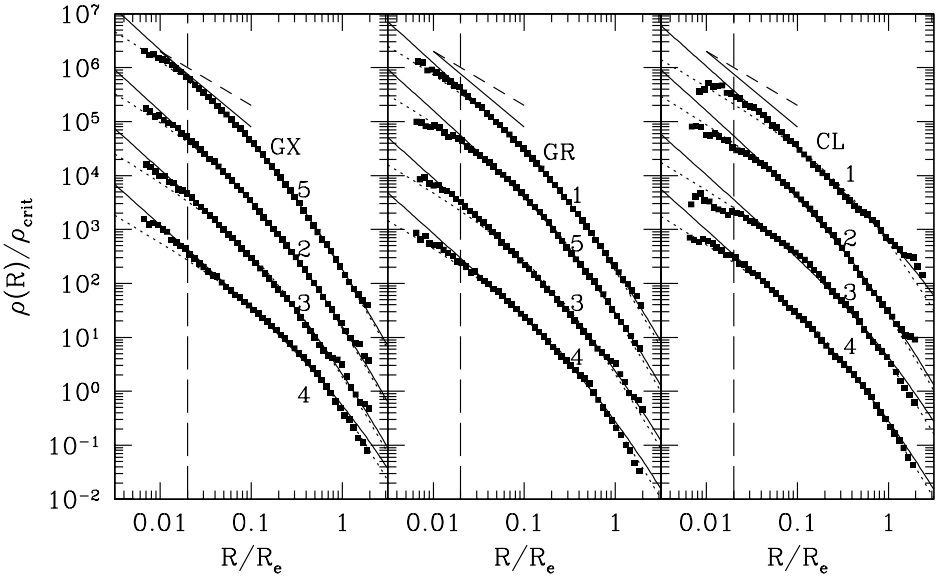

FIG. 6.—Radial density profiles in our triaxial model of the simulated halos of galaxy (*left*), group (*middle*), and cluster (*right*) masses. The solid and dotted curves represent fits to eq. (12) with $\alpha = 1.5$ and 1.0, respectively. For reference, we also show $\rho(R) \propto R^{-1}$ and $R^{-1.5}$ in dashed and solid lines. The vertical dashed lines indicate the force-softening length that corresponds to our resolution limit. For illustrative purposes, the values of the halo densities are multiplied by 1, 10^{-1}, 10^{-2}, and 10^{-3} from top to bottom in each panel. [*See the electronic edition of the Journal for a color version of this figure.*]

The best fits to equation (12) for each halo are shown in Figure 6 for $\alpha = 1.5$ (*solid lines*) and for $\alpha = 1.0$ (*dotted lines*). Up to the resolution limit of the halo simulations ($R/R_e \approx 0.02$), equation (12) yields a good fit both for $\alpha = 1$ and for $\alpha = 1.5$. If we compare the fits to the simulation data more carefully, however, $\alpha = 1$ works better for the halos of cluster mass and $\alpha = 1.5$ better for those of galactic mass, which is consistent with the finding of Jing & Suto (2000) in the spherical model (but see Fukushige & Makino 2001 for a different point of view).

We also introduce a concentration parameter in our triaxial model:

$$c_e \equiv \frac{R_e}{R_0} , \tag{14}$$

which is plotted in the upper panel of Figure 7 adopting $\alpha = 1.0$ (*crosses*) and $\alpha = 1.5$ (*filled circles*) in the fit. In what follows we will not address the issue related to the inner slope of the density profiles, and adopt $\alpha = 1$. It should be noted, however, that our statistical results presented in the next section can be readily applied to the $\alpha = 1.5$ case since the ratio $c_e(\alpha = 1.5)/c_e(\alpha = 1)$ is always close to $\frac{1}{2}$.

Before moving to the statistical analysis of halos in the cosmological simulations, we note that the value of R_e and thus that of c_e are dependent on our specific definition of Δ_e (eq. [13]). As the middle and bottom panels in Figure 7 indicate, both R_e/r_{vir} and c_e/c_{vir} (where c_{vir} is the ratio of the virial halo radius to the scale radius r_s in the spherical model) remain constant ($\approx$0.45) independently of the mass of the halos when we adopt equation (13) for Δ_e. This property is quite useful in applying our results for a variety of theoretical predictions, since for a halo of given virial mass M_{vir},

$$M_{vir} = \frac{4\pi}{3} r_{vir}^3 \Delta_{vir} \rho_{crit} , \tag{15}$$

the radius R_e in our triaxial model is easily computed. It is also known that the c_{vir} is a function of the halo mass (NFW; Eke, Navarro, & Steinmetz 2001) with the scatter described by the lognormal distribution function (Jing 2000; Bullock et al. 2001). Therefore, once the shape of a halo at a given mass is specified, the density profile of the halo is completely fixed. The statistical distribution function of the halo shape is discussed in the next section.

4. STATISTICS OF TRIAXIAL DENSITY PROFILES

High-resolution halo simulations, like those used in the last section, are well suited for studying the detailed internal structures of individual halos, but the number of such halos is too small for a statistical description. Therefore, we switch to the halo catalogs constructed from our cosmological simulations in order to study the probability distribution of the shape of halos. As emphasized in § 2, the cosmological simulations employ $N = 512^3$ particles in a 100 h^{-1} Mpc box and thus the mass resolution is even better than that of *individual halo simulations* in the original NFW paper, for instance.

We consider halos that contain more than 10^4 particles within the virial radius. The lower mass limits are 6.2×10^{12} and 2×10^{13} $M_\odot$ in the LCDM and SCDM models, respectively. We also consider three epochs at redshifts $z = 0$, 0.5, and 1.0 to examine the time dependence. At these redshifts, we have 2494, 2160, and 1534 halos in the LCDM model and 1806, 879, and 263 halos in the SCDM model, respectively.

4.1. *Probability Distribution of Axis Ratios*

Following the prescription presented in the last section, we determine the halo shapes at the isodensity surfaces with $A^{(3)} = 2500$. Since the typical radius of the surfaces is about $0.3r_{vir}$, they are well resolved in our cosmological simula-

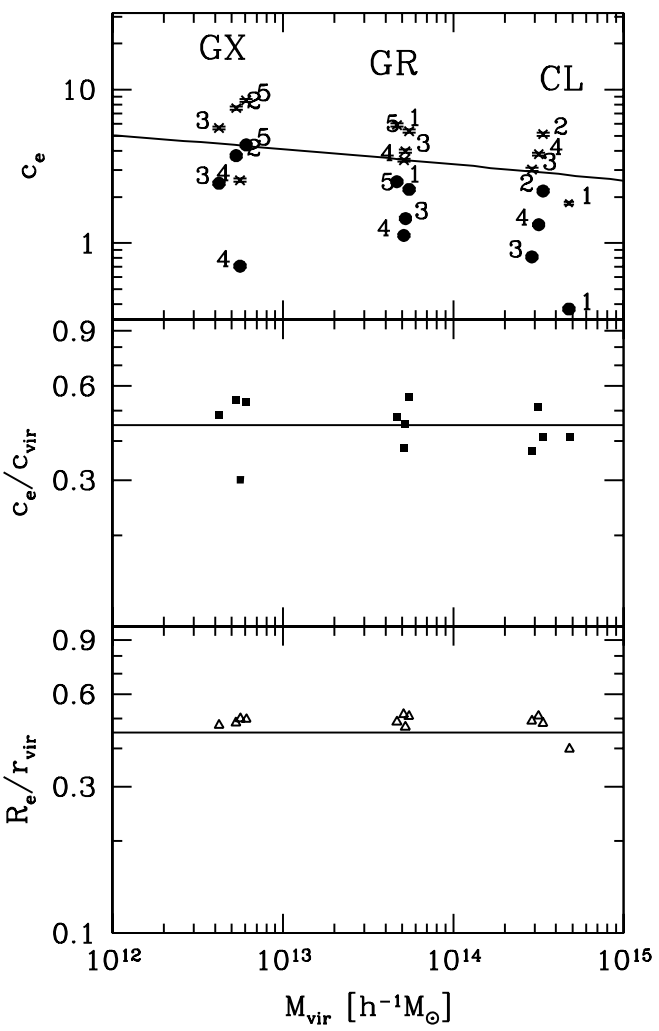

FIG. 7.—Fitting results of the triaxial model to 12 halos. *Top:* Concentration parameter c_e for $\alpha = 1$ (*crosses*) and for $\alpha = 1.5$ (*filled circles*); *middle:* ratio of c_e to that of the spherical counterpart $c_{\rm vir}$ for $\alpha = 1$; *bottom:* ratio of R_e to the virial radius $r_{\rm vir}$ in the spherical model. [*See the electronic edition of the Journal for a color version of this figure.*]

tions; the force-softening length is typically smaller by 1 order of magnitude.

The left panels of Figures 8 and 9 present the ratio a/c of the minor axis a to the major axis c for halos from the cosmological simulations in the LCDM and SCDM models, respectively; solid, dotted, and dashed histograms indicate the results for $10^4 \le N_{\rm halo} < 2 \times 10^4$, $2 \times 10^4 \le N_{\rm halo} < 6 \times 10^4$, $6 \times 10^4 \le N_{\rm halo}$, where $N_{\rm halo}$ is the number of particles within the virial radius of each halo; in those figures we use $M_4 \equiv N_{\rm halo}/10^4$, and thus $M_4 = 1$ corresponds to $M_{\rm vir} = 6.2 \times 10^{12}$ and $2.1 \times 10^{13}\ h^{-1}\ M_\odot$ for our LCDM and SCDM models). The top, middle, and bottom panels of Figures 8 and 9 show the results at $z = 0$, 0.5, and 1.0.

Two systematic trends are visible: the ratio is slightly larger for less massive halos and decreases at higher redshifts. This motivates us to attempt the following empirical scaling for the axis ratio a/c:

$$\tilde{r}_{ac} \equiv \left(\frac{a}{c}\right)_{\rm sc} = \left(\frac{a}{c}\right)\left(\frac{M_{\rm vir}}{M_*}\right)^{0.07[\Omega(z)]^{0.7}}, \qquad (16)$$

where M_* is the characteristic nonlinear mass at z so that the rms top-hat smoothed overdensity at the scale $\sigma(M_*, z)$ is $\delta_c = 1.68$. The M_* at $z = 0$, 0.5, and 1.0 are 9.4×10^{12}, 2.0×10^{12}, and $3.8 \times 10^{11}\ h^{-1}\ M_\odot$, respectively, for LCDM and 8.5×10^{12}, 9.7×10^{11}, and $1.4 \times 10^{11}\ h^{-1}\ M_\odot$, respectively, for SCDM.

Such scaled axis ratios $\tilde{r}_{ac}$ show a fairly universal distribution almost independently of the mass and the epoch (histograms in the right panels of Figs. 8 and 9). The *universal* probability distribution function of the ratio $\tilde{r}_{ac}$ is well fitted to the following Gaussian:

$$p(\tilde{r}_{ac})d\tilde{r}_{ac} = \frac{1}{\sqrt{2\pi}\sigma_s}\exp\left[-\frac{(\tilde{r}_{ac} - 0.54)^2}{2\sigma_s^2}\right]d\tilde{r}_{ac} \qquad (17)$$

with $\sigma_s = 0.113$.

Next we decompose the joint probability distribution function of the axis ratios as

$$\begin{aligned} p(a/c, b/c)d(a/c)d(b/c) &= p(a/c)d(a/c)p(b/c|a/c)d(b/c) \\ &= p(a/c)d(a/c)p(a/b|a/c)d(a/b) \end{aligned} \qquad (18)$$

in terms of the conditional probability distribution functions, $p(b/c|a/c)$ and $p(a/b|a/c)$. The second equality holds because once a/c is fixed, the distribution of a/b is uniquely determined from that of b/c. Since we have shown that the distribution function $p(a/c)$ is well approximated by equations (16) and (17), we compute the conditional probability distribution $p(a/b|a/c)$. Figures 10 and 11 plot the results for the LCDM and SCDM models, respectively. Different panels correspond to $p(a/b|a/c)$ for different ranges of a/c. Solid, dotted, and dashed histograms indicate $p(a/b|a/c)$ at $z = 0$, 0.5, and 1.0, respectively.

The conditional functions appear to be insensitive to the redshift. In both cosmological models, they are accurately fitted to

$$p(a/b|a/c) = \frac{3}{2(1 - r_{\rm min})}\left[1 - \left(\frac{2a/b - 1 - r_{\rm min}}{1 - r_{\rm min}}\right)^2\right] \qquad (19)$$

for $a/b \ge r_{\rm min}$, where $r_{\rm min} = a/c$ for $a/c \ge 0.5$ and $r_{\rm min} = 0.5$ for $a/c < 0.5$. $p(a/b|a/c) = 0$ for $a/b \ge r_{\rm min}$.

4.2. *Probability Distribution of the Concentration Parameter*

We apply the triaxial density profile (eq. [12]) obtained in the halo simulations to the halo catalogs in the cosmological simulations. Considering the resolution limits, we adopt $\alpha = 1$ and use the data points at $\eta < R_e < r_{\rm vir}$ in the fit, where η is the force-softening length (see § 2). Since we do not address the innermost structures of the halos and rather focus on the value of the concentration parameter c_e, this catalog has sufficient resolution to yield an unbiased estimate (e.g., Jing 2000; Bullock et al. 2001; Eke et al. 2001 for discussion). As already found in the spherical model (Jing 2000), the distribution of c_e in the triaxial model has a significant scatter even if the range of halo mass is fairly specified reflecting the dependence of the merging history of the individual halo.

The resulting probability distribution functions for c_e are presented in Figure 12, which are well fitted by the lognormal distribution:

$$p(c_e)dc_e = \frac{1}{\sqrt{2\pi}\sigma_{c_e}}\exp\left[-\frac{(\ln c_e - \ln \bar{c}_e)^2}{2\sigma_{\bar{c}_e}^2}\right]d\ln c_e \qquad (20)$$

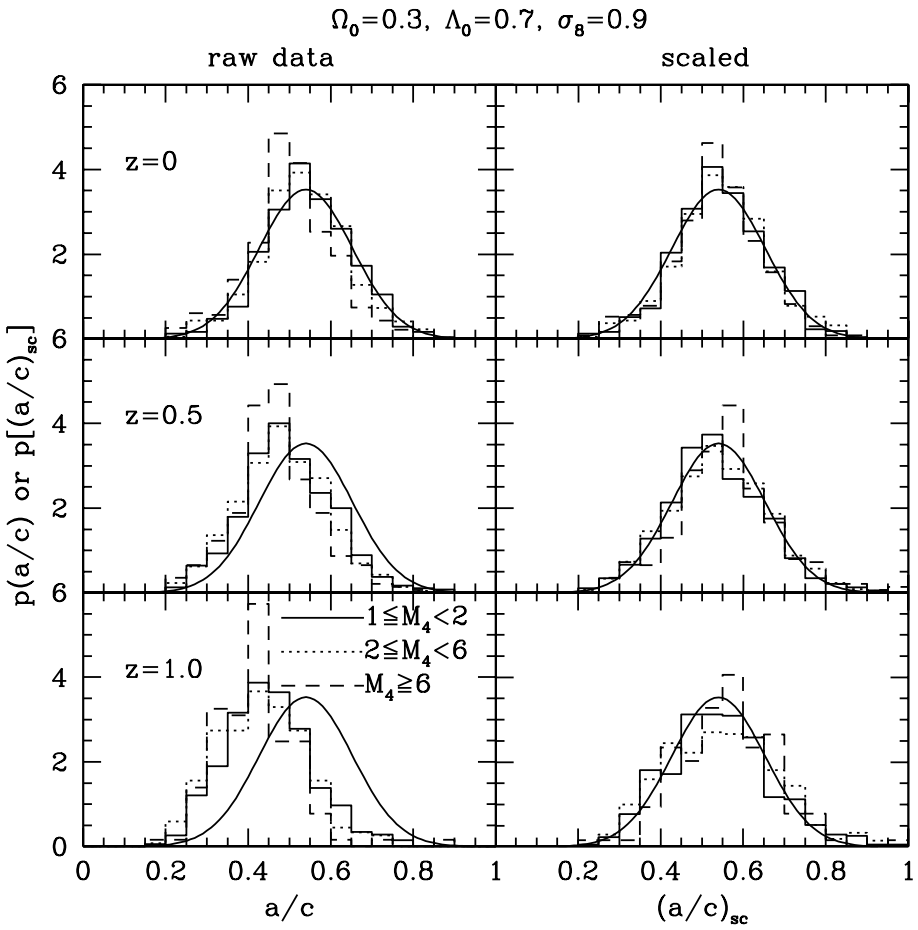

FIG. 8.—Distribution of the axis ratio a/c of the halos in the cosmological simulations of the LCDM model before (*left*) and after (*right*) the scaling described in the text. Top, middle, and bottom panels correspond to $z = 0$, 0.5, and 1.0, respectively. Solid, dotted, and dashed histograms indicate the results for halos that have the number of particles of $M_4 \equiv (N_{\rm halo}/10^4)$ within the virial radius. The smooth solid curves in all the panels represent our fit (eq. [17]). [*See the electronic edition of the Journal for a color version of this figure.*]

with a dispersion of $\sigma_{c_e} \approx 0.3$ in both the SCDM and LCDM models. The dispersion is slightly larger than the value estimated in the spherical model ($\approx$0.2) for equilibrium halos but is comparable to the value for all halos put together (Jing 2000). It should be noted here that despite the fact that the triaxial model is superior in describing the density distribution of halos, the scatter in c_e is comparable to the scatter of concentrations in spherical profile fits, which probably means that the scatter originates from the halo merger histories rather than nonsphericity of the halos.

The probability distribution (eq. [20]) is completed by specifying the mean of the concentration parameter $\bar{c}_e$. The result from our simulations is plotted in Figure 13 as a function of the halo mass at $z = 0$, 0.5, and 1.0. NFW proposed a semianalytic fitting formula for the concentration $c_{\rm vir}$ in the spherical model.[1] More recently, Bullock et al. (2001) have shown that in their LCDM model (the parameters are similar to those of our LCDM model here) $c_{\rm vir}$ of a given mass decreases with z proportionally as $(1 + z)^{-1}$. The redshift dependence is stronger than that predicted in the NFW recipe. Thus, Bullock et al. (2001) have proposed another recipe that successfully describes the concentration $c_{\rm vir}$. Since we have already shown that the ratio $c_e/c_{\rm vir}$ is almost constant (Fig. 7), it is interesting to see whether the formula of Bullock et al. (2001) also describes the behavior of c_e in our triaxial model.

In the LCDM model, we find that the redshift dependence of c_e for a given mass is approximately proportional to $(1 + z)^{-1}$, in good agreement with their result. In the SCDM model, however, our result of c_e shows a stronger redshift dependence than their prediction. It is also likely that the fitting formula of Bullock et al. (2001) was designed to fit spherical concentrations, $c_{\rm vir}$, and is not applicable to the nonspherical case because of the evolution of $c_e/c_{\rm vir}$.

Following NFW and Bullock et al. (2001), we propose a new fitting formula for $\bar{c}_e$ in the triaxial model:

$$\bar{c}_e(M, z) = A_e \sqrt{\frac{\Omega(z)}{\Omega(z_c)}} \left(\frac{1 + z_c}{1 + z}\right)^{3/2} . \qquad (21)$$

In the above, z_c is the *collapse* redshift of the halo of mass M (NFW):

$$\mathrm{erfc}\, \frac{\delta_c(z_c) - \delta_c}{\sqrt{2[\sigma^2(fM) - \sigma^2(M)]}} = \frac{1}{2} , \qquad (22)$$

[1] Originally NFW defined the concentration parameter as $c_{200} \equiv r_{200}/r_s$, where r_{200} is the radius within which the mean overdensity is $200\rho_{\rm crit}$. Their recipe, however, can be easily generalized to $c_{\rm vir}$, since r_{200}/r_v is almost constant for a given cosmology.

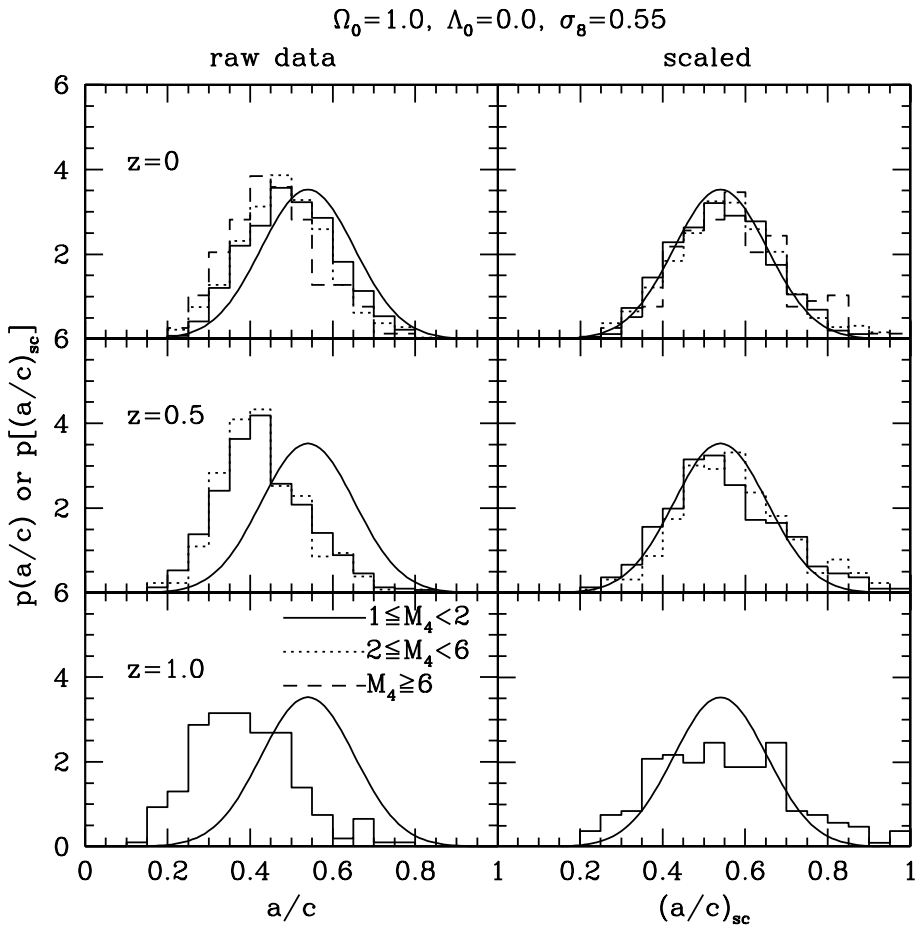

FIG. 9.—Same as Fig. 8, except for the halos in the SCDM simulations. [*See the electronic edition of the Journal for a color version of this figure.*]

where $\sigma(M)$ is the rms top-hat mass variance at $z = 0$, $\delta_c = 1.68$, $\delta_c(z) = 1.68/D(z)$, $D(z)$ is the linear growth factor, and $f = 0.01$. Solid lines in Figure 13 indicate the predictions of equation (21), implying that the formula describes our simulation results very accurately. In those plots, we adopt $A_e = 1.1$ and 1.0 for the LCDM and SCDM models, respectively.

We also made sure that the formula also agrees well with our halo simulations in the LCDM model, while the results appear 10%–20% higher (i.e., $A_e = 1.2$–1.3) than those of the cosmological simulations ($A_e = 1.1$). Considering both the typical 30% scatter in c_e and the limited number of high-resolution halos (12 in total), the above level of difference may not be interpreted so seriously at this point. In fact, the difference may be attributed partly to the fact that halos with significant substructures (like GR2) have been eliminated in the high-resolution halo samples (§ 2) while we have not attempted such a selection in the cosmological simulations. Indeed, Jing (2000) has noted that halos in equilibrium are systematically more centrally concentrated than those with significant substructures. We also note that most previous studies, including NFW and Eke et al. (2001), have preferentially selected isolated halos in resimulating with higher resolution, which would have fewer substructures and therefore have slightly higher concentration than average. If one is interested in halos nearly in equilibrium, the best-fit value of A_e should become 1.3. Since $c_e/c_{\rm vir}$ remains constant (Figs. 7 and 15), the fitting formula (eq. [21]) can also be used for predicting $c_{\rm vir}$ in CDM models.

Finally, we have checked whether the fitted values of R_e and c_e are dependent on the shapes of halos. Figure 14 presents the ratio of R_e to the virial radius $r_{\rm vir}$ as a function of the axis ratio a/b. Clearly, $R_e/r_{\rm vir}$ is independent of a/b and of the redshift (or equivalently the halo mass in units of M_*; see also Fig. 7) and approximately given by 0.45. Similarly, we find that $R_e/r_{\rm vir}$ is independent of b/c and a/c. On the other hand, the concentration parameter c_e is slightly dependent on the halo shape. Figure 15 indicates that halos with smaller a/c are less centrally concentrated.

In terms of the scaled axis ratio $(a/c)_{\rm sc}$ (eq. [16]), the ratio of the mean concentration c_e for a given $\tilde{r}_{ac} = (a/c)_{\rm sc}$ and the overall average $\bar{c}_e(M, z)$ (eq. [21]) is well approximated by

$$\frac{c_e[\tilde{r}_{ac}, M, z]}{\bar{c}_e(M, z)} = 1.35 \exp\left[-\left(\frac{0.3}{\tilde{r}_{ac}}\right)^2\right]. \qquad (23)$$

This fit is plotted with the solid line in Figure 15, which is in good agreement with the simulation data for different halo masses and in both the LCDM and SCDM models.

In this section, we used the halos identified from cosmological simulations that have $N > 10^4$ particles. The smallest halos are resolved much more poorly than the largest halos and the high-resolution halos (§ 3) that consist of

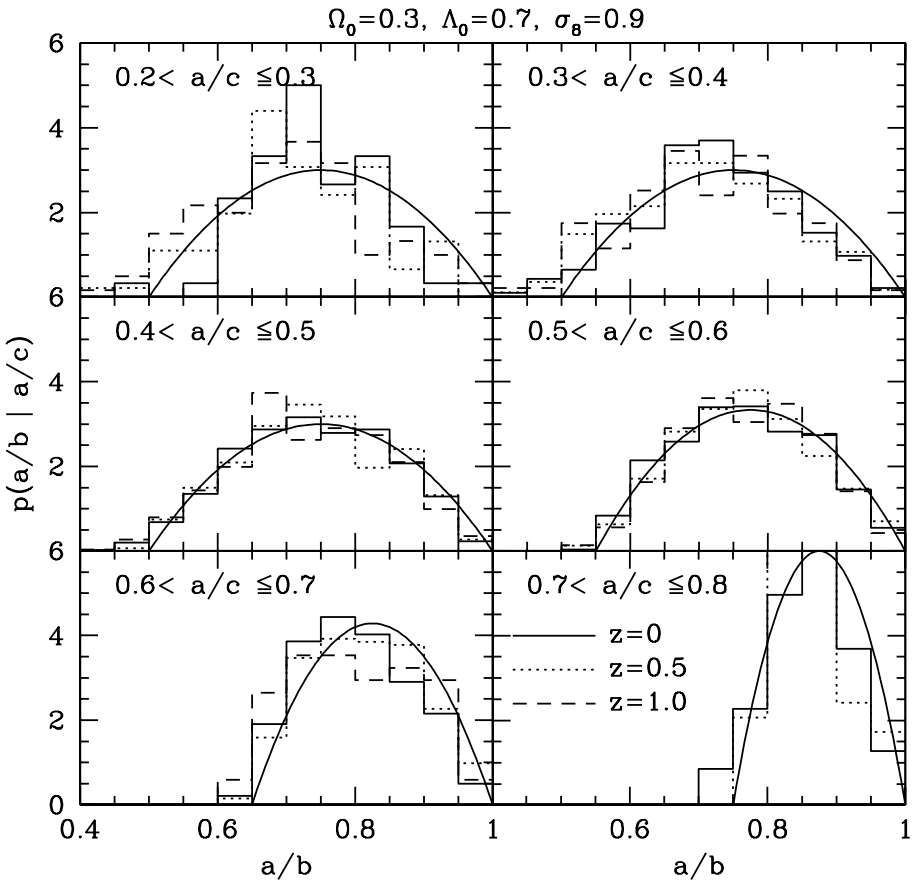

FIG. 10.—Conditional distribution of the axis ratio a/b of the halos in the cosmological simulations of the LCDM model for a given range of a/c. Halos at different redshifts are represented with different lines as indicated in the bottom right panel. The smooth solid curves in all the panels represent our fit (eq. [19]). [*See the electronic edition of the Journal for a color version of this figure.*]

$\sim 10^6$ particles. In order to make sure that our results are robust to the mass resolution, we repeat the same analysis of the axis ratios and the density profile by randomly selecting $N = 10^4$ particles from each of the 12 high-resolution halos of the previous section. The results are compared in Figure 16 with those obtained in the last section where we consider all particles. Both the axis ratios and the concentration of the randomly selected sample agree well with those of the original halo sample; the typical dispersion of the axis ratios between the two samples is $\sim 10\%$, and the concentration c_e of the randomly selected sample is slightly lower ($\sim 8\%$). This comparison indicates that the mass resolution does not affect our results in this section significantly.

5. SUMMARY AND DISCUSSION

This paper has presented a triaxial modeling of the dark matter halo density profiles extensively on the basis of the combined analysis of high-resolution halo simulations (12 halos with $N \sim 10^6$ particles within their virial radius) and large cosmological simulations (five realizations with $N = 512^3$ particles in a 100 h^{-1} Mpc box size). In particular, we found that the universal density profile discovered by NFW in the spherical model can be also generalized to our triaxial model description. Our triaxial density profile is specified by the concentration parameter c_e and the scaling radius R_0 (or the *virial* radius R_e in the triaxial modeling) as well as the axis ratios a/c and a/b.

We have obtained several fitting formulae for those parameters that are of practical importance in exploring the theoretical and observational consequences of our triaxial model (in doing so we have adopted $\alpha = 1$ since the precise value of the inner slope is difficult to reliably determine even with the resolution of the current simulations):

1. the mass and redshift dependence of the axis ratio, or equivalently the definition of the scaled axis ratio $\tilde{r}_{ac} \equiv (a/c)_{\rm sc}$: equation (16);
2. the probability distribution of the axis ratio $p(\tilde{r}_{ac})$: equation (17);
3. the conditional probability distribution of the axis ratios $p(a/b|a/c)$: equation (19);
4. the mean value of the concentration parameter $\bar{c}_e(M, z)$: equation (21);
5. the dependence of the concentration parameter on the axis ratio $\tilde{r}_{ac}$: equation (23); and
6. the probability distribution of the concentration parameter $p(c_e)$: equation (20).

Since $c_e/c_{\rm vir}$ remains constant (Figs. 7 and 15), the fitting formula (eq. [21]) can also be used for predicting $c_{\rm vir}$ in CDM models.

We have focused on the triaxial modeling and characterization of dark halos in the present paper and plan to show specific applications elsewhere. Nevertheless, it would be worthwhile to mention several important examples of the current model.

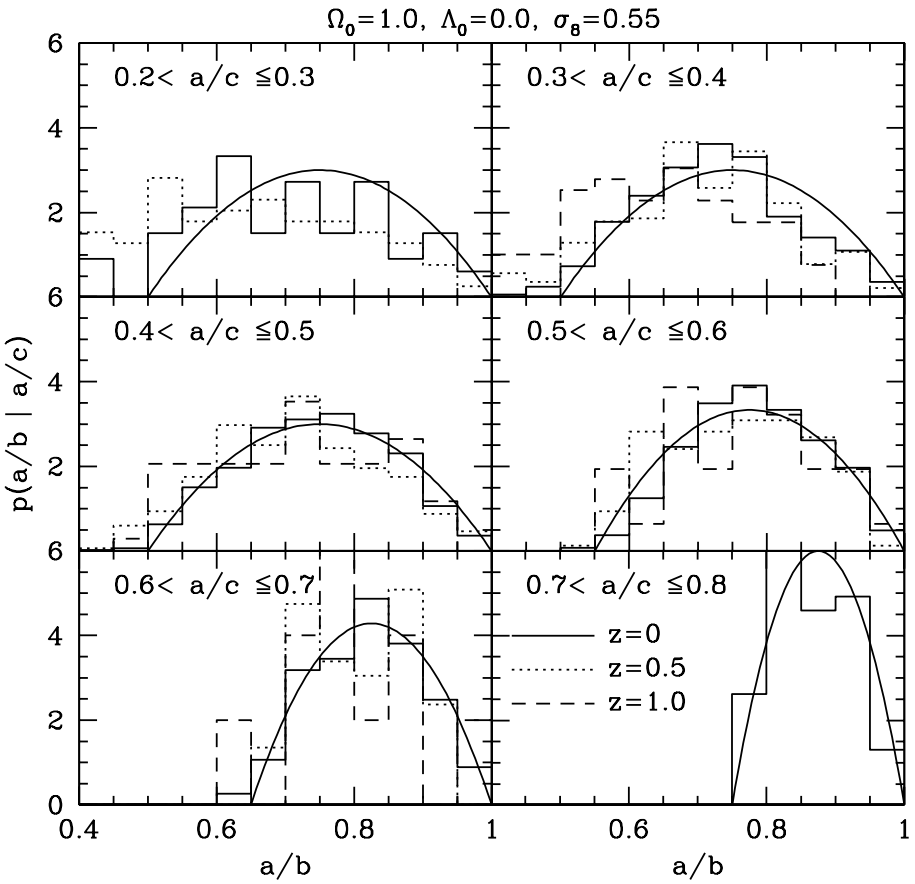

FIG. 11.—Same as Fig. 10, except for the halos in the SCDM simulations. [*See the electronic edition of the Journal for a color version of this figure.*]

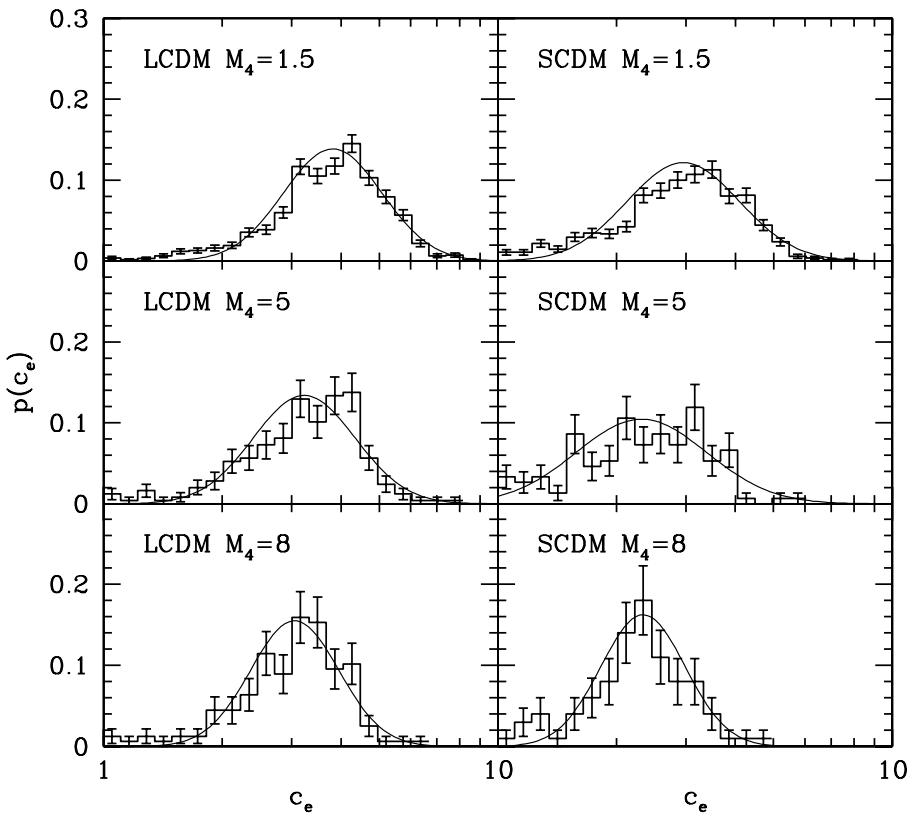

FIG. 12.—Distribution of the concentration c_e of the halos in the LCDM (*left*) and in the SCDM (*right*) models for different halo mass $M_4 \equiv (N_{\rm halo}/10^4)$. The smooth solid curves represent our lognormal fit (eq. [20]).

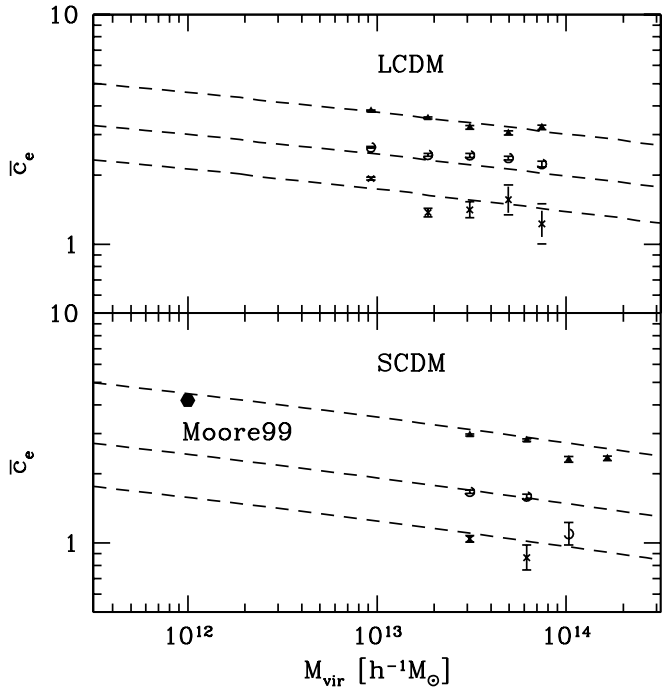

FIG. 13.—Mean of the concentration $\bar{c}_e$ as a function of the virial mass in the LCDM and SCDM models. The solid curves represent our fitting formula (eq. [21]) at $z = 0$, 0.5, and 1.0 from top to bottom. The data point, labeled Moore99, is taken from the result of Moore et al. (1999) and is scaled according to our fitting formula (eq. [21]). [*See the electronic edition of the Journal for a color version of this figure.*]

The results of the paper are applicable in a fairly direct manner to the following three areas. (1) The weak and strong lens statistics: the comparison with the weak lensing observations provides information on the degree of triaxiality of observed clusters, mainly at outer regions. In addition, the frequency of the lensing arc is known to be sensitive to the nonsphericity of the halo mass profile, especially in the central regions (e.g., Bartelmann et al. 1998; Meneghetti et al. 2000, 2001; Molikawa & Hattori 2001; Oguri 2002). (2) Predictions of the nonlinear clustering of dark matter based on the halo model (e.g., Mo, Jing, & Börner 1997; Ma & Fry 2000; Hamana et al. 2001; Kang et al. 2002): the high-order statistics of clustering, e.g., the three-point correlation and the bispectrum, should be quite sensitive to the nonsphericity. (3) Dynamics of galactic satellites: recently this has been argued to be very sensitive to the nonsphericity of the host halo (e.g., Ibata et al. 2001). The combination of those three approaches would even yield a direct test of the cold dark matter paradigm (Spergel & Steinhardt 2000; Yoshida et al. 2000).

Of course, the nonsphericity of dark matter halos is critical to understanding that of the gas density profile of clusters of galaxies. Since gasdynamics is characterized by the isotropic pressure tensor, gas does not directly follow the dark matter distribution in halos. In fact, most hydrodynamic simulations of galaxy clusters suggest that the gas distribution is generally rounder than that of dark matter. Nevertheless, we would like to mention a couple of important examples where the nonsphericity in the gas distribution has crucial and observable consequences. (4) The gas

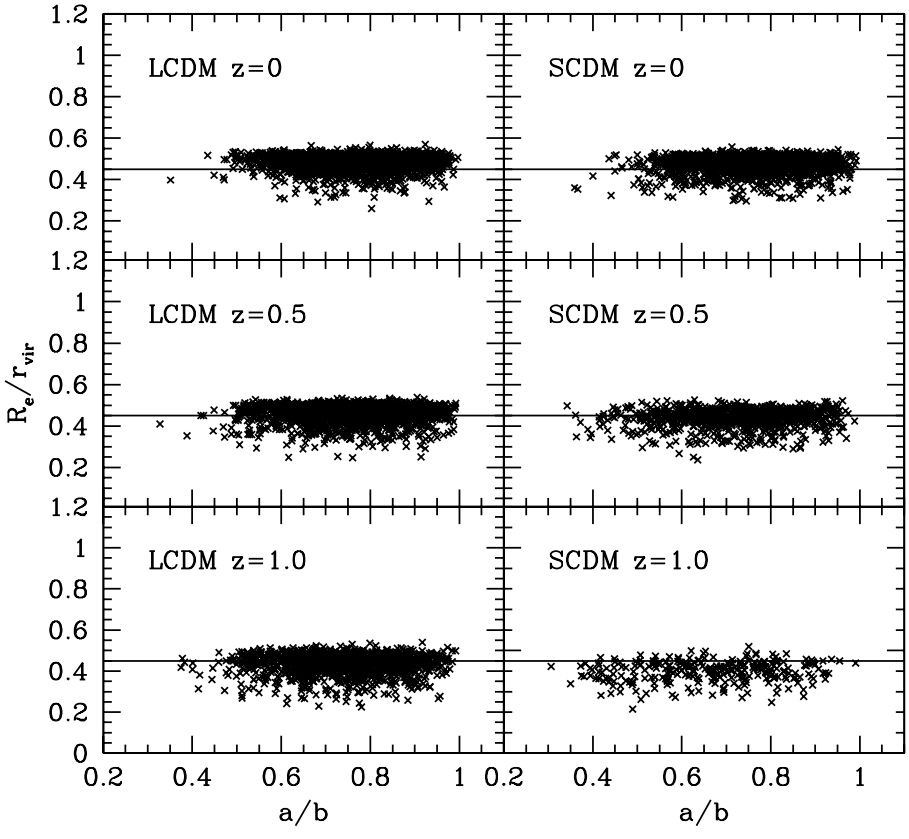

FIG. 14.—Ratio of R_e to the virial radius for halos with different shapes in the LCDM (*left*) and SCDM (*right*) models at different redshifts

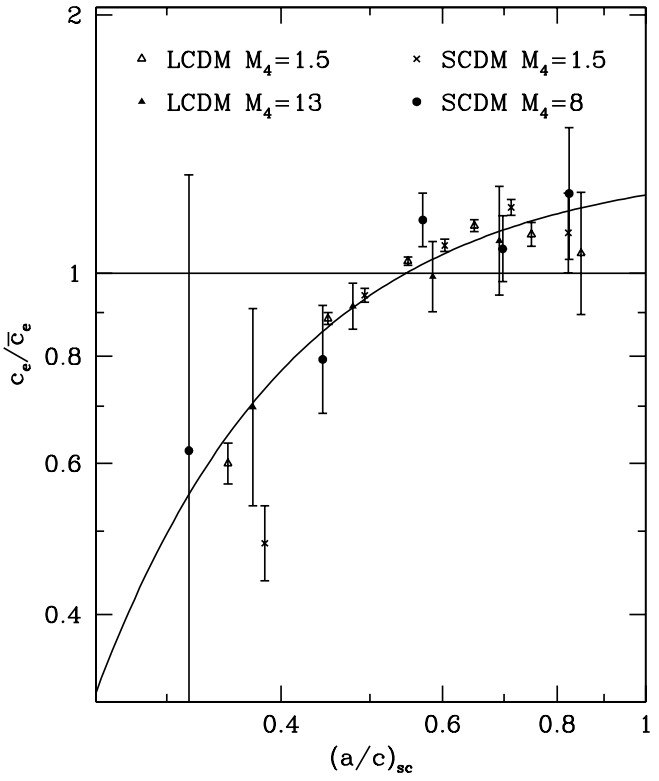

FIG. 15.—Dependence of the ellipsoid concentration c_e on the scaled axis ratio $(a/c)_{sc}$. Different symbols denote the results of halos of different mass ($N_{halo} = 10^4 M_4$ particles) in the LCDM and SCDM models. The smooth solid curve represents our fitting formula (eq. [23]). [*See the electronic edition of the Journal for a color version of this figure.*]

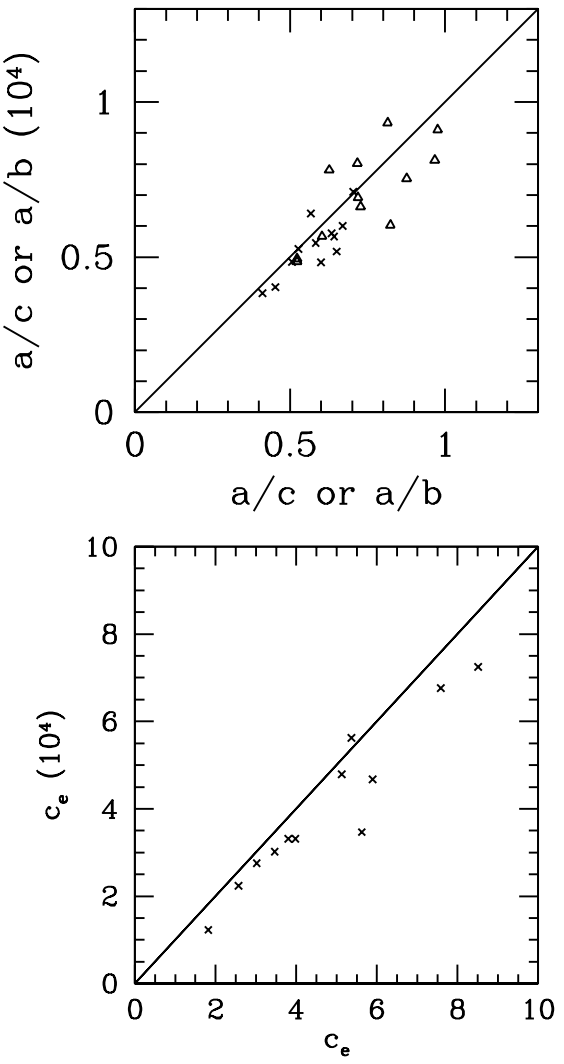

FIG. 16.—Axis ratios a/c (*crosses*, *upper panel*) and b/c (*triangles*, *upper panel*) and the concentration c_e (*lower panel*) of a subsample of halo particles randomly selected from the 12 high-resolution halos compared with those of the whole sample (abscissa). Each halo in the subsample has $N_p = 10^4$ particles.

and temperature profiles of X-ray clusters: almost all previous analytical models for the X-ray profiles of galaxy clusters have adopted the spherical approximation perhaps because of the lack of any specific model for the nonsphericity. Since our triaxial model specifies the gravitational potential of the hosting halos, one may compute the gas or temperature profiles, with an additional assumption of the hydrostatic equilibrium, for instance, as performed in the NFW model (e.g., Makino, Sasaki, & Suto 1998; Suto, Sasaki, & Makino 1998; Komatsu & Seljak 2001). If combined with the observed surface brightness distribution of clusters, one may in principle solve for the gas and temperature profiles simultaneously for a given nonspherical distribution of dark matter (Silk & White 1978; Yoshikawa & Suto 1999; Zaroubi et al. 1998). (5) The systematic bias and statistical distribution of the Hubble constant estimated via the Sunyaev-Zeldovich effect: in view of the ongoing observational projects, it is of vital importance to reevaluate the reliability of the estimates taking account of the nonsphericity effect of the clusters. With the above modeling of the gas and temperature profiles for individual clusters, one may discuss the statistical properties of the estimates of the Hubble constant (e.g., Fox & Pen 2002), combining the extensive fitting formula for the probability distribution functions of the triaxial model parameters and the halo mass function (e.g., Sheth & Tormen 1999; Jenkins et al. 2001).

We thank an anonymous referee for helpful comments on the earlier manuscript. Numerical simulations presented in this paper were carried out at ADAC (the Astronomical Data Analysis Center) of the National Astronomical Observatory, Japan, and at KEK (High Energy Accelerator Research Organization, Japan). Y. P. J. was supported in part by the One-Hundred-Talent Program, by NKBRSF (G19990754), and by NSFC (10125314), and Y. S. was supported in part by the grant-in-aid from Monbu-Kagakusho (07CE2002, 12640231) and by the Supercomputer Project (00-63) of KEK.

REFERENCES

Bardeen, J. M., Bond, J. R., Kaiser, N., & Szalay, A. S. 1986, ApJ, 304, 15
Barnes, J., & Efstathiou, G. 1987, ApJ, 319, 575
Bartelmann, M., Huss, A., Colberg, J. M., Jenkins, A., & Pearce, F. R. 1998, A&A, 330, 1
Birkinshaw, M., Hughes, J. P., & Arnaud, K. A. 1991, ApJ, 379, 466
Bryan, G. L., & Norman, M. 1998, ApJ, 495, 80
Bullock, J. S. 2001, preprint (astro-ph/0106380)
Bullock, J. S., Kolatt, T. S., Sigad, Y., Somerville, R. S., Kravtsov, A. V., Klypin, A. A., Primack, J. R., & Dekel, A. 2001, MNRAS, 321, 559
Buote, D. A., & Xu, G. 1997, MNRAS, 284, 439
Davis, M., Efstathiou, G., Frenk, C. S., & White, S. D. M. 1985, ApJ, 292, 371

Dubinski, J. 1994, ApJ, 431, 617
Efstathiou, G., Davis, M., Frenk, C. S., & White, S. D. M. 1985, ApJS, 57, 241
Eke, V. R., Navarro, J. F., & Steinmetz, M. 2001, ApJ, 554, 114
Fox, D. C., & Pen, U. 2002, ApJ, 574, 38
Fukushige, T., & Makino, J. 1997, ApJ, 477, L9
———. 2001, ApJ, 557, 533
Hamana, T., Yoshida, N., Suto, Y., & Evrard, A. E. 2001, ApJ, 561, L143
Hernquist, L., & Katz, N. 1989, ApJS, 70, 419
Hockney, R. W., & Eastwood, J. W. 1981, Computer Simulation Using Particles (New York: McGraw Hill)
Ibata, R., Lewis, G. F., Irwin, M., Totten, E., & Quinn, T. 2001, ApJ, 551, 294
Inagaki, Y., Suginohara, T., & Suto, Y. 1995, PASJ, 47, 411
Jenkins, A., Frenk, C. S., White, S. D. M., Colberg, J. M., Cole, S., Evrard, A. E., Couchman, H. M. P., & Yoshida, N. 2001, MNRAS, 321, 372
Jing, Y. P. 2000, ApJ, 535, 30
Jing, Y. P., & Fang, L. Z. 1994, ApJ, 432, 438 (JF94)
Jing, Y. P., Mo, H. J., Borner, G., & Fang, L. Z. 1995, MNRAS, 276, 417
Jing, Y. P., & Suto, Y. 1998, ApJ, 494, L5
———. 2000, ApJ, 529, L69
Kang, X., Jing, Y. P., Mo, H. J., & Börner, G. 2002, preprint (astro-ph/0201124)
Keeton, C. R., & Madau, P. 2001, ApJ, 549, L25
Kitayama, T., & Suto, Y. 1997, ApJ, 490, 557
Klypin, A., Kravtsov, A. V., Bullock, J. S., & Primack, J. R. 2001, ApJ, 554, 903
Komatsu, E., & Seljak, U. 2001, MNRAS, 327, 1353
Lacey, C., & Cole, S. 1994, MNRAS, 271, 676
Lahav, O., et al. 2002, MNRAS, submitted (astro-ph/0112162)
Ma, C., & Fry, J. N. 2000, ApJ, 531, L87
Makino, N., Sasaki, S., & Suto, Y. 1998, ApJ, 497, 555
Meneghetti, M., Bolzonella, M., Bartelmann, M., Moscardini, L., & Tormen, G. 2000, MNRAS, 314, 338
Meneghetti, M., Yoshida, N., Bartelmann, M., Moscardini, L., Springel, V., Tormen, G., & White, S. D. M. 2001, MNRAS, 325, 435
Mo, H. J., Jing, Y. P., & Börner, G. 1997, MNRAS, 286, 979
Molikawa, K., & Hattori, M. 2001, ApJ, 559, 544
Moore, B., Governato, F., Quinn, T., Stadel, J., & Lake, G. 1998, ApJ, 499, L5
Moore, B., Quinn, T., Governato, F., Stadel, J., & Lake, G. 1999, MNRAS, 310, 1147
Navarro, J. F., Frenk, C. S., & White, S. D. M. 1996, ApJ, 462, 563
———. 1997, ApJ, 490, 493
Oguri, M. 2002, ApJ, 573, 51
Oguri, M., Taruya, A., & Suto, Y. 2001, ApJ, 559, 572
Seljak, U. 2002, MNRAS, submitted (astro-ph/0111362)
Sheth, R. K., & Tormen, G. 1999, MNRAS, 308, 119
Silk, J., & White, S. D. M. 1978, ApJ, 226, L103
Spergel, D. N., & Steinhardt, P. J. 2000, Phys. Rev. Lett., 84, 3760
Suginohara, T., & Suto, Y. 1992, ApJ, 396, 395
Suto, Y., Cen, R. Y., & Ostriker, J. P. 1992, ApJ, 395, 1
Suto, Y., Sasaki, S., & Makino, N. 1998, ApJ, 509, 544
Thomas, P. A., et al. 1998, MNRAS, 296, 1061
Warren, M. S., Quinn, P. J., Salmon, J. K., & Zurek, W. H. 1992, ApJ, 399, 405
Yoshida, N., Springel, V., White, S. D. M., & Tormen, G. 2000, ApJ, 544, L87
Yoshikawa, K., Itoh, M., & Suto, Y. 1998, PASJ, 50, 203
Yoshikawa, K., & Suto, Y. 1999, ApJ, 513, 549
Zaroubi, S., Squires, G., Hoffman, Y., & Silk, J. 1998, ApJ, 500, L87